International Journal of High Speed Electronics and Systems
(2024) 2440063 (12 pages)

DOI: 10.1142/S0129156424400639

Mid-Infrared Spectrometer Based on Tunable Photoresponses in $Pdse_2$

Jea Jung Lee
Department of Electrical Engineering, Yale University, New Haven, CT 06511, USA
jeajung.lee@yale.edu

Adi Levi* and Doron Naveh†
Faculty of Engineering, Bar-Ilan University, Ramat-Gan 52900, Israel
**adi.levi1@biu.ac.il*
†*doron.naveh@biu.ac.il*

Fengnian Xia‡
Department of Electrical Engineering, Yale University, New Haven, CT 06511, USA
fengnian.xia@yale.edu

AQ: Please provide ORCID ID for all authors. Note that the http address should be in valid format, leading to the correct webpage.

Received 19 April 2024
Accepted 31 May 2024
Published

Mid-infrared (mid-IR) photodetection is important for various applications, including biomedical diagnostics, security, chemical identification, and free-spacing optical communications. However, conventional "photon" mid-IR photodetectors require liquid nitrogen cooling (i.e., MCT). Furthermore, acquiring mid-IR spectra usually involves a complex and expensive Fourier Transform Infrared spectrometer, a tabletop instrument consisting of a meter-long interferometer and MCT detectors, which is not suitable for mobile and compact device applications. In this work, we present tunable photoresponsivity in the mid-IR wavelength in palladium diselenide ($PdSe_2$) – molybdenum disulfide (MoS_2) heterostructure field-effect transistors (FETs), operating at room temperature. Furthermore, we applied a tunable membrane cavity to modulate the Fabry–Pérot resonance to modulate the absorption spectrum of the device layer. We used a robust polyetherimide (PEI) membrane with CVD-grown graphene to electrically tune the membrane structure. For the next step, we will integrate the $PdSe_2$-based photodetector and tunable membrane to increase detection sensitivity and spectrum tunability to realize the 'learning'-based spectroscopy.

Keywords: Photoresponse; palladium diselenide; mid-infrared; 'learning'-based spectroscopy; Fabry–Pérot cavity.

‡Corresponding author.

1. Introduction

Optical detection and spectroscopy in the mid-infrared (mid-IR) wavelength regime are extensively investigated due to their importance in various applications, including biomedical sensing, security, environmental monitoring, and free-space optical communications. For example, most molecules have their vibrational resonances in this wavelength range, so mid-IR spectroscopy has been widely used in chemical and biomedical identification [1]. Additionally, the mid-IR range is also promising for free-spacing optical communications because it contains an atmospheric transmission window ($35\,\mu m$ and $813\,\mu m$) where the absorption from air molecules is suppressed [2]. Traditional mid-IR detection devices exploited the interband "photo" absorption, such as mercury cadmium telluride (MCT) [3]. However, they usually require liquid nitrogen cooling, making their miniaturizing challenging. On the other hand, microbolometers, leveraging a "thermal" detection mechanism, can be used for room-temperature mid-IR detection [4]. However, due to their low operational speed, detection sensitivity, and spectrum tunability, their application in spectroscopy is limited.

Recently, Yuan *et al.* [5]. demonstrated a single-device spectrometer that proposed the concept of learning-based spectroscopy. The bandgap of the black phosphorus (BP) is tuned by the electric field, allowing for the reconfigurability of spectral response in the infrared range. Researchers leveraged the reconfigurable spectral response to "learn" the photoresponsivity matrix of the BP device. The photoresponsivity matrix learned from multiple known spectra can be utilized to reconstruct the unknown spectrum by sampling the photoresponse. This research denotes that we can directly interpret the spectrum of light without cumbersome components such as interferometer or grating with a single device. However, the BP single-device spectrometer still requires liquid-nitrogen cooling. Thus, the room-temperature operational principle needs to be investigated. Moreover, BP quickly degrades in the air [6]. Thus additional encapsulating layers such as hexagonal boron nitride (hBN) are necessary for its stable operation [7], which renders the fabrication of a spectrometer challenging. For this reason, air-stable materials are highly preferred.

The newly rediscovered transition metal dichalcogenide (TMD) palladium diselenide ($PdSe_2$) has a widely tunable bandgap, depending on its thickness, and it is stable in the air [8, 9]. Additionally, $PdSe_2$ can be synthesized on a large scale [10–12], which is important for applications. These recent progress and properties make that $PdSe_2$ is a promising material candidate for future mid-IR spectroscopy.

In this work, we observed a negative temperature coefficient of resistivity (TCR) and bolometric photoresponse with a mid-IR laser from a $PdSe_2$-MoS_2 heterostructure device. Furthermore, we fabricate a tunable membrane structure to modulate the absorption of the device layer via Fabry–Pérot resonance. Finally,

AQ: Please check and approve the short title.

we suggest a new scheme for a tunable learning-based spectrometer operating at room temperature by combining a $PdSe_2$ device and a flexible membrane structure.

2. Operational Principle

This section outlines the operational principles of the mid-IR spectrometer. Section 2.1 explains the basic concept of a "learning-based" photodetection algorithm. Section 2.2 describes the approach for tuning the photoresponse spectrum and increasing the photoresponse sensitivity with a tunable membrane structure.

2.1. *Learning based photodetection*

Learning-based photodetection leverages the tunable photoresponses to acquire the responsivity matrix, which is used to decode unknown optical information [5, 13]. Figure 1 shows the schematic of the learning-based photodetection mechanism. Figure 1(a) illustrates the learning process. The photoresponse (e.g., photocurrent or photovoltage) of a spectrometer device can be tuned by a degree of freedom (e.g., electric displacement field). The responsivity vector $\boldsymbol{R}_{\boldsymbol{\lambda},\boldsymbol{D}_i}$ of the spectrometer, which depends on the incident light wavelength (λ) at the fixed degree of freedom (D_i), is "learned" from the photoresponses to multiple known spectra $\boldsymbol{P}_{\boldsymbol{T}_i}$ by utilizing Eq. (1) [5]. Measurements through multiple values of degree of freedom (D_i),

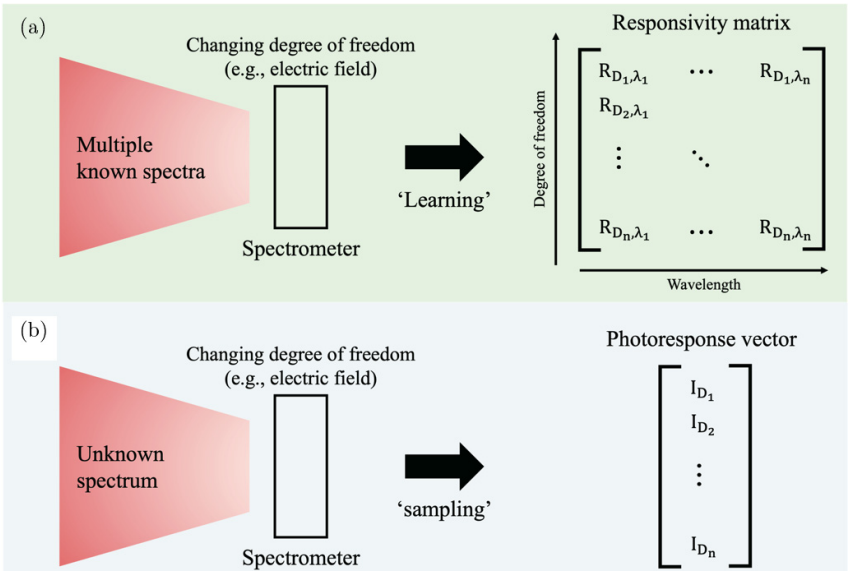

Fig. 1. Schematics of a 'learning'-based photodetection mechanism. (a) The "Learning" process; (b) The 'Sampling' process. Adapted from Ref. 5 with modifications.

we can produce entire responsivity matrix $\boldsymbol{R_{\lambda,D}}$.

$$\begin{pmatrix} I_{T_1} \\ I_{T_2} \\ I_{T_3} \\ \vdots \\ I_{T_n} \end{pmatrix} = \begin{pmatrix} P_{T_1,\lambda_1} & P_{T_1,\lambda_2} & \cdots & P_{T_1,\lambda_n} \\ P_{T_2,\lambda_1} & P_{T_2,\lambda_2} & & \\ \vdots & \vdots & \ddots & \\ P_{T_n,\lambda_1} & P_{T_n,\lambda_2} & & P_{T_n,\lambda_n} \end{pmatrix} \begin{pmatrix} R_{\lambda_1} \\ R_{\lambda_2} \\ R_{\lambda_3} \\ \vdots \\ R_{\lambda_n} \end{pmatrix}. \tag{1}$$

Figure 1(b) demonstrates the sampling process of the learning-based photodetection. For the incident light with an unknown spectrum, the photoresponse in the spectrometer is sampled as a function of the degree of freedom. The sampling process generates the measured photoresponse vector $\boldsymbol{I_D} = \langle \boldsymbol{I_{D_1}}, \boldsymbol{I_{D_2}}, \ldots, \boldsymbol{I_{D_n}} \rangle$. Finally, the unknown incident spectrum power density vector $\boldsymbol{P_\lambda}$ can be reconstructed by the following equation [5]:

$$\begin{pmatrix} P_{\lambda_1} \\ P_{\lambda_2} \\ P_{\lambda_3} \\ \vdots \\ P_{\lambda_n} \end{pmatrix} = \left[\begin{pmatrix} R_{D_1,\lambda_1} & R_{D_1,\lambda_2} & \cdots & R_{D_1,\lambda_n} \\ R_{D_2,\lambda_1} & R_{D_1,\lambda_2} & & \\ \vdots & \vdots & \ddots & \\ R_{D_n,\lambda_1} & R_{D_n,\lambda_2} & & R_{D_n,\lambda_n} \end{pmatrix} \right]^{-1} \begin{pmatrix} I_{D_1} \\ I_{D_2} \\ I_{D_3} \\ \vdots \\ I_{D_n} \end{pmatrix}. \tag{2}$$

In summary, by using a "learning-based" photodetection algorithm, the spectroscopy function can be realized without advanced optical components such as interferometers or movable grating.

2.2. *Tunable membrane structure*

Photoresponse in $PdSe_2$ at mid-IR regime mostly comes from the bolometric effect [9, 14]. Thus, reducing thermal conduction is one of the most important keyframes when designing the device structure [15]. Therefore, suspending two-dimensional materials on the membrane with low thermal conductance [16] largely increases bolometric photoresponse since heat dissipation to the surroundings gets suppressed.

Suspending two-dimensional materials on the membrane also enables tuning the spectral response of the $PdSe_2$ device. If the membrane is electrically conductive, the electric field can easily tune the membrane height [17]. Tunable membrane height changes the absorbance spectrum of the two-dimensional material device via the Fabry–Pérot cavity [18]; thus, the bolometric photoresponsivity can be tuned. This tuning mechanism is important since a bolometric photoresponse basically detects the temperature dependence of the conductance, thus it is hard to tune it electrically [4]. Figure 2 is the schematic of the Fabry–Pérot cavity of tunable membrane structure.

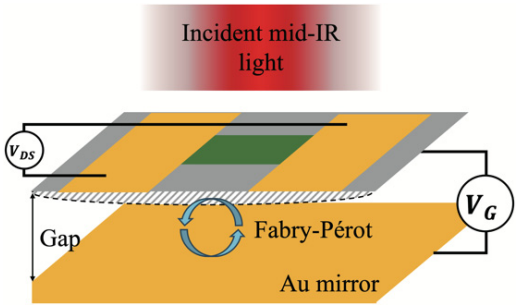

Fig. 2. Schematic of Fabry–Pérot cavity with tunable membrane.

3. Device Fabrication

This section describes the device fabrication process and method. Section 3.1 reports the fabrication process of the $PdSe_2$-MoS_2 heterostructure. The process for tunable membrane structure is described in Sec. 3.2.

3.1. *Fabrication process for $PdSe_2$-MoS_2 heterostructure*

Figure 3(a) is a schematic of the heterostructure device fabrication process. After identifying the suitable $PdSe_2$ and MoS_2 flakes by the mechanical exfoliation method [19], we used a polydimethylsiloxane (PDMS) stamp covered with polycarbonate (PC) to stack and transfer the $PdSe_2$-MoS_2 heterostructure [20, 21]. First, we pick-up the $PdSe_2$ flask, heating the substrate at 120°C. Second, we pick-up the MoS_2 flake in the same way. Then, the heterostructure was transferred onto a highly doped Si wafer covered with a 90 nm SiO_2 layer at 180°C. Finally, metal electrodes (10 nm Ti/50 nm Au) were deposited by electron-beam lithography and

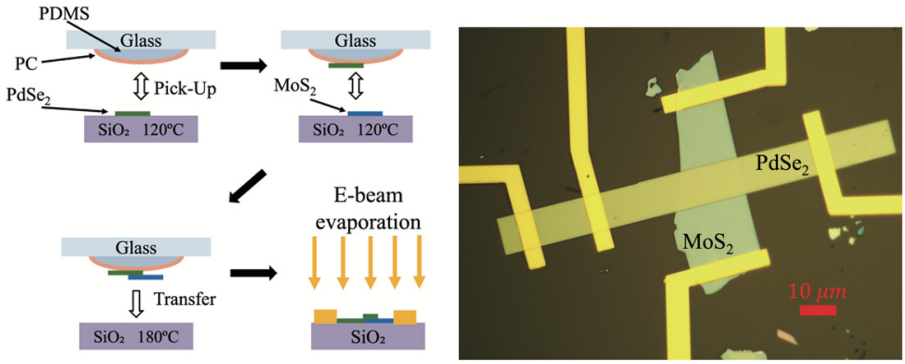

(a) (b)

Fig. 3. Schematics of $PdSe_2$-MoS_2 heterostructure device fabrication process. (b) Optical micrograph of fabricated heterostructure device.

electron-beam evaporation process. Figure 3(b) is the optical microscope image of the heterostructure device. The thickness of $PdSe_2$ is around 65 nm, which is thick enough to have a narrow band gap to absorb mid-IR light [8]. The overlapped area between $PdSe_2$ and MoS_2 is around 165 μm^2.

3.2. *Fabrication processes for membrane structure*

Figure 4(a) is a schematic of the process to construct the electrically modulated membrane structure. We used a flexible polyetherimide (PEI) membrane with a chemical vapor deposition (CVD) grown graphene [22]. PEI has a low thermal conductivity [23]. Thus, it is appropriate to integrate with a bolometric photodetector. However, an additional conducting layer (e.g., graphene) is necessary to modulate the height because of the insulating behavior of the PEI.

We first prepare the substrate with a cavity for the PEI membrane. The cavity at the center of the substrate is patterned by electron-beam lithography and then etched using buffered oxide etchant (BOE). For the next step, a thermal evaporator deposits the gold mirror in the cavity and the electrode in contact with CVD-grown graphene for tuning the membrane.

On the other hand, we spin-coated PEI (3 wt%) CVD-grown graphene on the Cu foil. Then, we used the APS-100 solution to etch the Cu, floating the PEI/Graphene

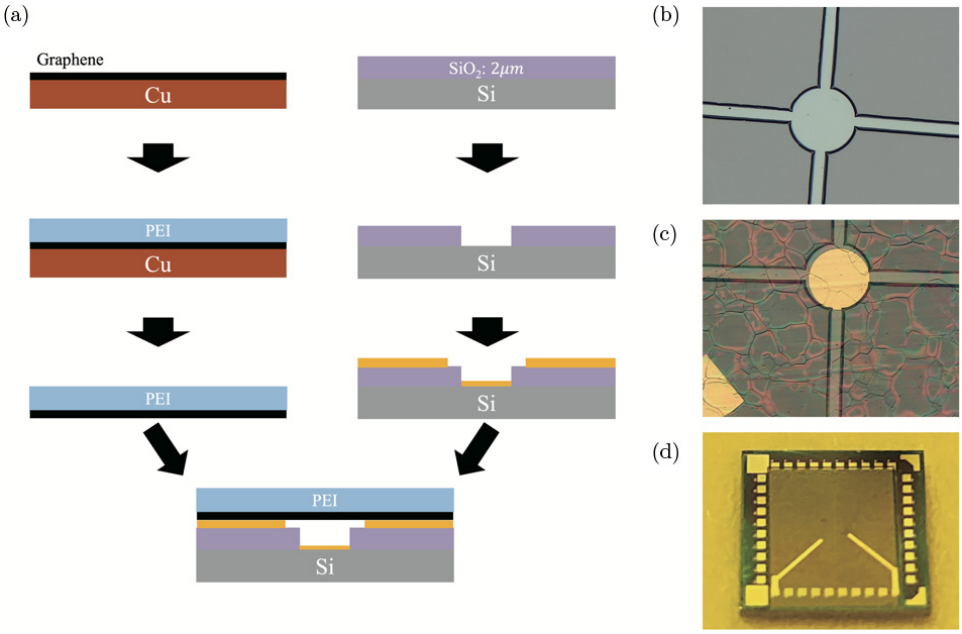

Fig. 4. (a) Schematic of the tunable membrane structure fabrication processes. (b) and (c) Optical microscope images of cavity structure after the BOE process (b) and transferring of PEI membrane (c). (d) Photo of the final device.

membrane. Finally, the PEI/Graphene membrane was transferred to the substrate we described above.

Figures 4(b) and 4(c) illustrate the device after the BOE process and transferring PEI membrane, respectively. The final fabricated device is shown in Fig. 4(d).

4. Experimental Results at Room-Temperature

This section describes the experimental results of the $PdSe_2$-MoS_2 heterostructure (Sec. 4.1) and electrically modulated membrane (Sec. 4.2). All the experiments were conducted at room temperature.

4.1. *Electrical and optoelectrical measurements of the $PdSe_2$-MoS_2 heterostructure*

Figure 5(a) shows the schematics of the electrical connection of the heterostructure device. Global back gate voltage is biased through the highly doped silicon substrate. Both $PdSe_2$ and MoS_2 show n-type behavior in Figs. 5(b) and 5(c). $PdSe_2$-MoS_2 heterostructure device (drain-source bias is connected through the two different materials) also shows n-type dominant behavior, but current increase (V_G from -12 to $-9V$) and decrease (V_G from -9 to $0V$) can be observed in Fig. 5(d). The energy barrier at the heterostructure tuned by the gate voltage causes those changes.

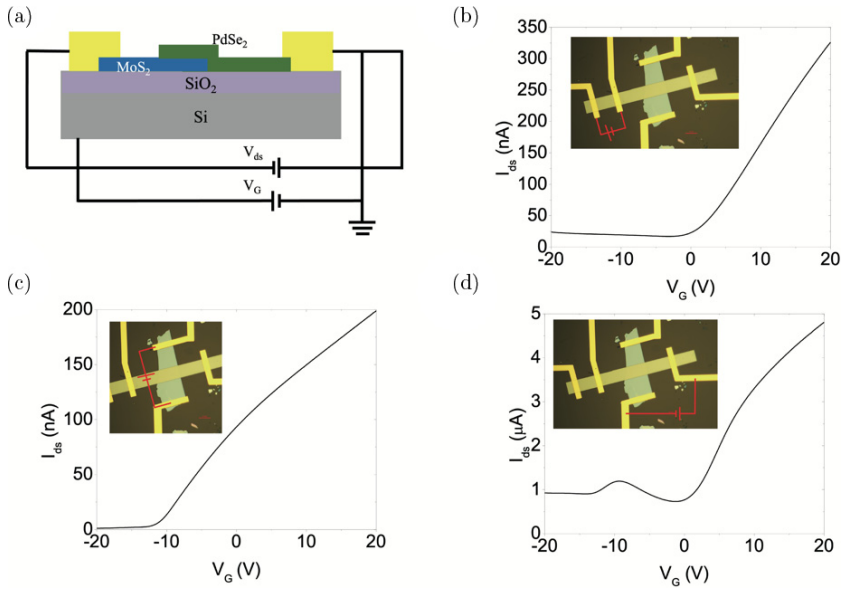

Fig. 5. (a) Schematic of device connection for electrical measurements. (b)–(d) Transfer curves of $PdSe_2$ (b) and MoS_2 (c) with $V_{ds} = 10\,mV$. (d) Transfer curve of heterostructure device with $V_{ds} = 3\,V$.

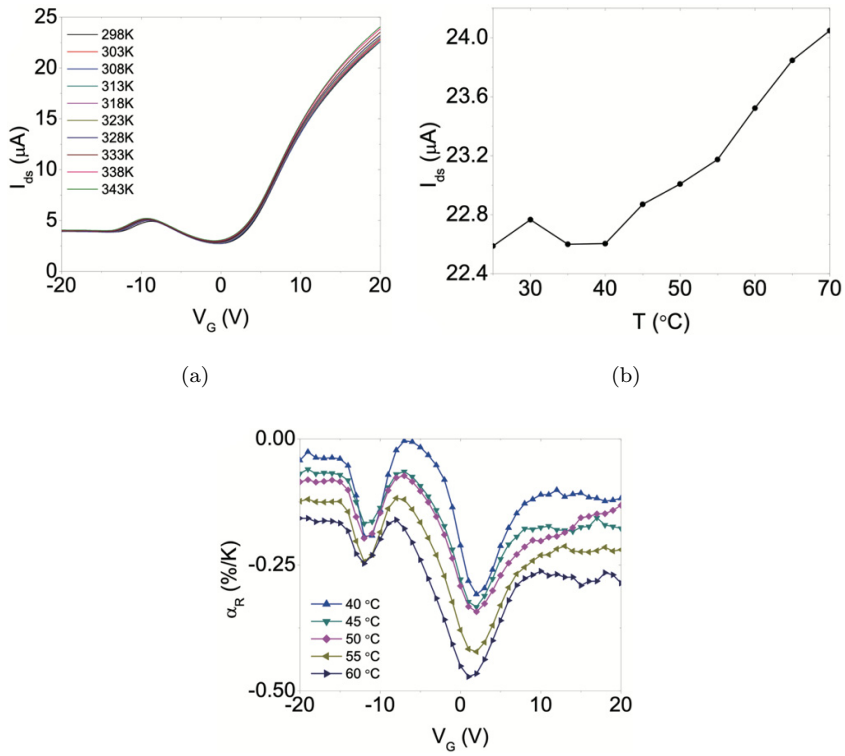

(a) (b)

(c)

Fig. 6. (a) Transfer curves of heterostructure device measured from 25°C to 70°C. (b) Darin-source current as a function of the temperature when $V_G = 20V$. (c) Temperature coefficient of resistance (TCR) as a function of gate voltage.

4.1.1. *Negative temperature coefficient of resistance (TCR)*

To study the transport properties of the $PdSe_2$-MoS_2 heterostructure, temperature-dependent transfer curves were measured from 25°C to 70°C in Fig. 6(a). The current increased with increasing temperature overall, indicating that temperature increases the conductance of the heterostructure device (Fig. 6(b)). Since mid-IR light heats the device, changing its conductance, incident mid-IR light can be detected with the change of the current. Bolometric photoresponsivity R_{bolo} can be described as shown in Eq. (3), where P_{dev} is the incident power on the device, I_{ph} is the output photocurrent, G is thermal conductance, α_R is temperature coefficient of resistance (TCR), I_{ds} is device bias current, η is absorbance of the device, ω is angular frequency of modulation of the radiation, and τ is thermal response time [15].

$$R_{bolo} = \frac{I_{ph}}{P_{dev}} = \frac{I_{ds}\alpha_R\eta}{G(1+\omega^2\tau^2)^{1/2}}(A/W). \tag{3}$$

Since the sign of I_{ds} is determined by the measurement condition and all other elements in Eq. (3) are positive, the sign of the bolometric photoresponsivity R_{bolo} is determined by the sign of TCR.

Generally, TCR (α_R) is defined as

$$\alpha_R = \frac{1}{R}\frac{dR}{dT}. \tag{4}$$

According to the definition, the TCR as a function of the gate voltage is shown in Fig. 6(c). The TCR can be tuned from 0% to $-0.5\%\,\mathrm{K}^{-1}$ by the gate voltage with the two dips. Negative TCR (reduction of resistance with increased temperature) means the bolometric photocurrent produced by mid-IR light, which is discussed in the following section, has a positive value.

4.1.2. *Photoresponses in $PdSe_2$-MoS_2 heterostructure device*

The tunable TCR of heterostructure makes it desirable for bolometric photodetection to use spectroscopy of mid-IR light. To evince the tunability of the $PdSe_2$-MoS_2 bolometer via gate bias, we measured photocurrent as a function of gate voltage with $5\,\mu m$, $7.7\,\mu m$ and $10\,\mu m$ lasers. The schematic of the set-up for the photocurrent measurement is illustrated in Fig. 7(a). The Lock-in amplifier collects the voltage inputs $\mathrm{V_{ph}}$, synchronized with chopper frequency, and it is converted to photocurrent with pre-amplifier gain G_{gain} as shown in the following equation [24]:

$$I_{ph} = 2\pi\sqrt{2}V_{ph}/4G_{gain}. \tag{5}$$

Photoresponsivity, then, calculated with photocurrent with Eq. (3), where incident power on the device P_{dev} is $58\,\mu W(5\,\mu m), 66\,\mu W(7.7\,\mu m)$, or $34\,\mu W(10\,\mu m)$ and presented in Fig. 7(b). The photoresponses generally increase as larger drain-source current I_{ds} is utilized, because of the relatively small TCR of the heterostructure device. However, the photoresponsivity is highly dependent on the gate voltage.

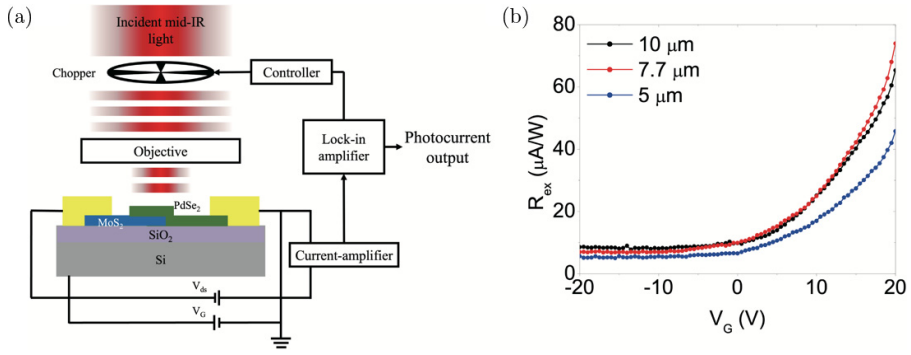

Fig. 7. (a) Schematic of the photocurrent measurement set-up. Adapted from [24] with modifications. (b) Photoresponsivity of $PdSe_2$-MoS_2 heterostructure device depends on the gate voltage with $5\,\mu m, 7.7\,\mu m$, and $10\,\mu m$ lasers.

4.2. *Membrane modulation by electrical field*

From Eq. (3), bolometric photoresponsivity is affected by the optical absorbance of the device. Therefore, the photoresponse of the bolometer can be tuned by modulating the cavity height between the membrane and gold mirror because of the Fabry–Pérot interference. The membrane structure we rendered in Fig. 4(d) is largely tunable by the electrical field applied to the cavity [22]. We observed that Newton's rings moved when we applied the electric field; thus, we noticed that the membrane was modulated electrically [25] (Fig. 8).

Since we used $2\,\mu m$ SiO_2 layer and deposited 100 nm gold in cavity fabrication, the Fabry–Pérot resonance wavelength $\lambda = 4d$ is in the mid-IR range (d is cavity height between the gold mirror and PEI membrane) [26]. Therefore, this electrically tunable membrane structure is appropriate to establish a "learning-based" mid-IR photodetector.

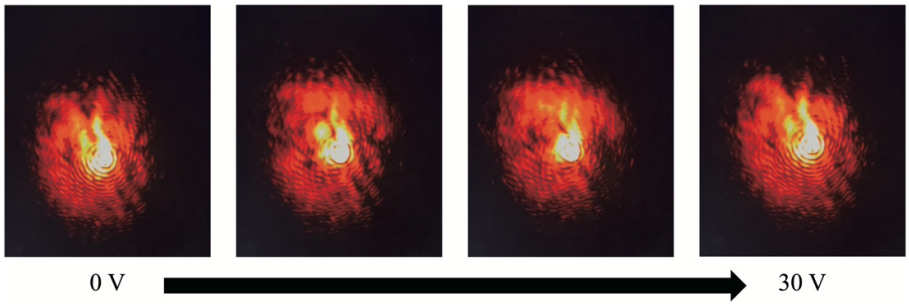

Fig. 8. Optical microscope images showing the change of Newton's rings on the PEI membrane. These indicate the PEI membrane is modulated by biased voltage.

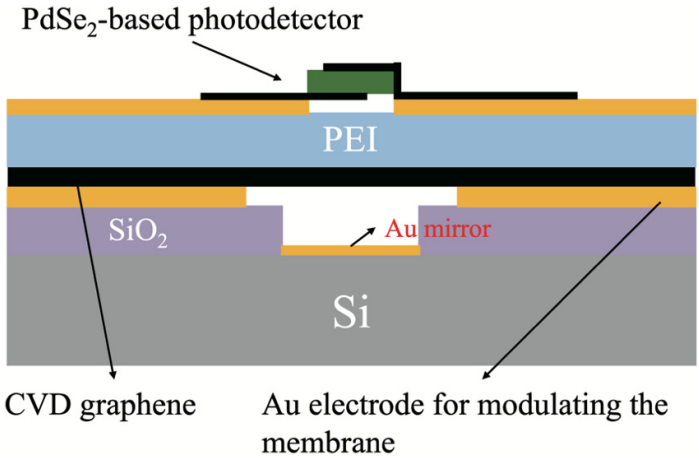

Fig. 9. Schematic of $PdSe_2$-based photodetector integrated with tunable Fabry–Pérot membrane cavity structure.

5. Conclusion and Future Works

This work reports the gate-tunable photoresponses in a $PdSe_2$-based photodetector in a mid-IR regime and proposes a method to tune the bolometric photoresponse using the Fabry–Pérot cavity with an electrically modulated membrane. We fabricated the $PdSe_2$-MoS_2 heterostructure device and PEI membrane cavity. All the measurements were conducted at the room-temperature or higher ($\sim$70°C). We observed the gate-tunable bolometric photoresponses and membrane height modulation, laying the foundation for the realization of sensitive and largely tunable mid-IR photodetector for spectroscopy applications.

In the next steps, we will combine a $PdSe_2$-based photodetector and membrane structure to increase the photoresponse by suppressing heat dissipation to surroundings and widening the modulation range by using a tunable Fabry–Pérot membrane cavity, as illustrated in Fig. 9.

Acknowledgments

Fengnian Xia and Jea Jung Lee thank the National Science Foundation for support through grant NSF-BSF 2150561. Jea Jung Lee is grateful for support from Yale Cleanroom, YINQE, Mikhael Guy at Yale Center for Research Computing, Bingchen Deng, and Shaofan Yuan.

References

1. Caffey, D., *et al.*, *Recent results from broadly tunable external cavity quantum cascade lasers*. SPIE OPTO, ed. Vol. 7953 (SPIE, 2011).
2. Green, A. E. S. and M. Griggs, Applied Optics. **2**(6): p. 561–570 (1963).
3. Rogalski, A., Reports on Progress in Physics. **68**(10): p. 2267 (2005).
4. Kruse, P. W., *Uncooled Thermal Imaging Arrays, Systems, and Applications*. Vol. 51 (SPIE, 2001).
5. Yuan, S., *et al.*, Nature Photonics. **15**(8): p. 601–607 (2021).
6. Kim, J.-S., *et al.*, Scientific Reports. **5**(1): p. 8989 (2015).
7. Chen, X., *et al.*, Nature Communications. **8**(1): p. 1672 (2017).
8. Oyedele, A. D., *et al.*, Journal of the American Chemical Society. **139**(40): p. 14090–14097 (2017).
9. Wen, S., *et al.*, ACS Applied Nano Materials. **6**(18): p. 16970–16976 (2023).
10. Zeng, L.-H., *et al.*, Advanced Functional Materials. **29**(1): p. 1806878 (2019).
11. Wei, M., *et al.*, npj 2D Materials and Applications. **6**(1): p. 1 (2022).
12. Xu, W., *et al.*, Nano Research. **13**(8): p. 2091–2097 (2020).
13. Yuan, S., *et al.*, Science. **379**(6637): p. eade1220 (2023).
14. Zhang, R., *et al.*, Advanced Optical Materials. **11**(23): p. 2301055 (2023).
15. Yadav, P. V. K., *et al.*, Sensors and Actuators A: Physical. **342**: p. 113611 (2022).
16. Youngblood, N. and M. Li, Nanophotonics. **6**(6): p. 1205–1218 (2017).
17. Holsteen, A. L., A. F. Cihan, and M. L. Brongersma, Science. **365** (6450): p. 257–260 (2019).
18. Wei, H., *et al.*, Small. **17**(35): p. 2100446 (2021).
19. Novoselov, K. S., *et al.*, Science. **306**(5696): p. 666–669 (2004).
20. Shin, S., *et al.*, Carbon. **111**: p. 215–220 (2017).

21. Wang, L., *et al.*, Science. **342**(6158): p. 614–617 (2013).
22. Khan, A. U., *et al.*, Advanced Materials. **33**(2): p. 2004053 (2021).
23. Lee, H. L., *et al.*, Physical Chemistry Chemical Physics. **16**(37): p. 20041–20046 (2014).
24. Yuan, S., *et al.*, ACS Photonics. **7**(5): p. 1206–1215 (2020).
25. Vaughan, M., *The Fabry-Perot Interferometer*: *History*, *Theory*, *Practice and Applications*. 1st ed. (Routledge, New York, 1989).
26. Abdullah, A., *et al.*, Scientific Reports. **13**(1): p. 3470 (2023).